Available online at www.sciencedirect.com
ScienceDirect
Journal of Magnesium and Alloys xxx (xxxx) xxx
www.elsevier.com/locate/jma

Full Length Article

Exceptional thermal stability and enhanced hardness in a nanostructured Mg-Gd-Y-Zn-Zr alloy processed by high pressure torsion

Wanting Sun[a,e], Yang He[d], Xiaoguang Qiao[a,*], Xiaojun Zhao[b], Houwen Chen[b], Nong Gao[c], Marco J. Starink[c], Mingyi Zheng[a,*]

[a] School of Materials Science and Engineering, Harbin Institute of Technology, Harbin 150001, China
[b] College of Materials Science and Engineering, Chongqing University, Chongqing 400044, China
[c] Materials Research Group, School of Engineering, University of Southampton, Southampton SO17 1BJ, United Kingdom
[d] Center for Composite Materials and Structures, Harbin Institute of Technology, Harbin 150001, China
[e] Department of Industrial and Systems Engineering, The Hong Kong Polytechnic University, Hung Hom, Hong Kong, China

Received 23 February 2022; received in revised form 17 April 2022; accepted 17 April 2022
Available online xxx

Abstract

A Mg-8.2Gd-3.8Y-1.0Zn-0.4Zr (wt.%) alloy is processed by solution treatment and high pressure torsion (HPT) at room temperature to produce a nanostructured light material with high hardness. The stability of this alloy is subsequently tested through isochronal annealing for 0.5 h at 373 K to 673 K. The results reveal a thermal stability that is vastly superior to that of conventional Mg-based alloys processed by severe plastic deformation: the grain size remains at around 50 nm on heating to 573 K, and as the temperature is increased to 673 K, grain growth is restricted to within 500 nm. The stability of grain refinement of the present alloy/processing combination allowing grain size to be limited to 55 nm after exposure at 573 K, appears to be nearly one order of magnitude better than for the other SPD processed Mg-RE type alloys, and 2 orders of magnitude better than those of SPD processed RE-free Mg alloys. This superior thermal stability is attributed to formation of co-clusters near and segregation at grain boundaries, which cause a thermodynamic stabilization of grain size, as well as formation of β-Mg_5RE equilibrium phase at grain boundaries, which impede grain growth by the Zener pinning effect. The hardness of the nanostructured Mg-Gd-Y-Zn-Zr alloy increases with increasing annealing temperature up to 573 K, which is quite different from the other SPD-processed Mg-based alloys. The high hardness of 136 HV after annealing at 573 K is mainly due to solute segregation and solute clustering at or near grain boundaries.

Keywords: Mg-RE alloy; High pressure torsion; Thermal stability; Grain growth; Solute segregation; Phase transformation.

1. Introduction

Magnesium alloys have bright application prospects in electronic, automotive and space fields owing to the low density, high specific strength and specific stiffness [1]. For conventional Mg-based alloys, inherent drawbacks such as low strength, inferior ductility and poor thermal stability, restrict their applications. It is now well established that the addition of rare earth (RE) elements into Mg-based alloys causes a remarkable improvement in strength due to solid solution and precipitation hardening [2]. Moreover, in Mg-RE alloys the Zener pinning effect of thermal stable RE-containing intermetallics on grain boundaries impedes grain growth at elevated temperatures, leading to excellent heat resistance [3,4], whilst also solute segregation to grain boundaries has been shown to influence grain growth and recrystallization [5,6].

High plastic deformation causing grain refinement and high dislocation densities is another effective approach to enhance the mechanical properties of materials. High pressure torsion (HPT) is a kind of severe plastic deformation (SPD)

* Corresponding authors.
E-mail addresses: xgqiao@hit.edu.cn (X. Qiao), zhenghe@hit.edu.cn (M. Zheng).

https://doi.org/10.1016/j.jma.2022.04.003

technique that can produce polycrystalline metals with ultrafine or nanosized grains with a large fraction of grain boundaries having high angles of misorientation at ambient temperature [7]. However, due to high densities of defects (including vacancies, dislocations and boundaries) created during HPT deformation, the obtained nanostructured system is in a non-equilibrium state, and softening due to grain growth and recovery occurs at relatively low temperatures, leading to a strength loss [8]. Works on AZ type (Mg-Al-Zn) alloys processed by different SPD methods, indicate that the thermal stability depends strongly on the grain size, alloy composition, and processing parameters [9–12]. The equal channel angular pressing (ECAP)-processed AZ31 (Mg-3Al-1Zn-0.3Mn (wt.%)) alloy with grain size of 0.7 μm experienced faster grain growth than the counterpart with grain size of 2.5 μm processed by conventional methods [10]. The friction stir processed (FSP) AZ91(Mg-8.3Al-0.9Zn-0.25Mn-0.2Si (wt.%)) alloy had a thermal stability that was superior to that of an ECAP processed AZ31 alloy with similar grain size, which was attributed to the presence of different types of precipitates [9,10,12]. As compared to nanocrystalline pure Mg with an average grain size of 65 nm, an Mg-5Ti (at.%) sample with the same grain size produced by mechanically alloying showed a better thermal stability, with an ultrafine grain size of 145 nm after annealing at 350 °C for 1 h [13]. However, the latter sample showed abnormal grain growth and the formation of the bimodal microstructure was ascribed to the inhomogeneous distribution of solute/impurity atoms at grain boundaries even though there was no direct observation provided for Ti segregation [13]. In contrast, research on the thermal stability of Mg-RE alloys has been mainly focused on the coarse microstructure that is obtained by conventional thermomechanical processing, i.e. with grain sizes in the micron range [3,4,14], while very limited data on annealing response for the SPD-processed Mg-RE alloys are available. Recent work has shown that the microstructure stability of the ultrafine grained Mg-1.2Zn-1.7Y-0.53Al-0.27Mn (wt.%) alloy processed by hot rolling and FSP is better than that of the AZ31 alloy, and this was interpreted to be due to the presence of W phase, Laves C15 and β-Mn precipitates in the former [15]. The Mg-10Gd (wt.%) alloy processed by HPT for 5 turns exhibited a dramatic decrease in dislocation density on exposure in the temperature range from 100 to 220 °C, and the mean grain size remained 100 nm up to 260 °C, which was interpreted to be due to the precipitation of stable β phase [16]. Different grain size led to various dislocation substructures and grain boundary volume fractions, which in turn governed precipitation behavior [16,17].

We feel that the thermal stability of nanostructured Mg-based alloys may be improved through appropriate alloying and thermomechanical processing, and particularly segregation and clustering of RE elements near grain boundaries may be exploited to improve stability [18]. To improve understanding of this technologically important field, this paper reports a detailed analysis of the thermal stability of a Mg-based alloy with high RE content produced by solution heat treatment followed by HPT at room temperature. It has been shown that for various ternary and higher order alloy systems combining alloying elements that have larger and smaller sizes[1] [19,20] than the main element (i.e. in this case Mg) particularly stimulates the formation of co-clusters in grains and at grain boundaries [21,22]. For this reason, Zn, which has a good solid solubility in Mg-RE alloys, is also added. (Further, also Zr is added because it generally provides grain refinement and increase in tensile strength without a loss of ductility for conventionally produced Al- and Mn-free Mg alloys [23].) Thermodynamic calculations were performed to assess solubility of RE alloying elements and Zn in Mg and on this basis Mg-8.2Gd-3.8Y-1.0Zn-0.4Zr (wt.%) was chosen as an alloy that meets the criteria. The solution treated and subsequently HPT-processed material was subjected to isochronal annealing at different temperatures and the relation between phase transformations, grain growth and hardness evolution after annealing was revealed.

2. Experimental procedures

A Mg-8.2Gd-3.8Y-1Zn-0.4Zr (wt.%) ingot was fabricated by direct-chill casting, and then subjected to solid solution treatment at 783 K for 12 h, immediately followed by water quenching. Disks having a diameter of 10.0 mm and a thickness of 1.0 mm were machined from the solutionized billet, and ground with abrasive papers on both sides to a final thickness of ~0.85 mm with parallel broad surfaces. HPT processing of these disks was performed under 6 GPa up to 10 turns using a rotation speed of 1 rpm under quasi-constrained conditions at room temperature [24]. The HPT-processed samples were isochronally annealed at four different temperatures, i.e. 473 K, 573 K, 623 K and 673 K for 0.5 h followed by water quenching, respectively.

Microstructural examinations were conducted on a FEI Talos F200X transmission electron microscope (TEM) operated at 200 kV accelerating voltage. In order to investigate local composition variations in the alloy, high resolution high-angle annular dark-field scanning transmission electron microscopy (HAADF-STEM) was performed on a FEI Titan G^2 60–300 ChemiSTEM, equipped with a Cs probe corrector and a Super-X EDS with four windowless silicon-drift detectors, operated at 300 kV. The TEM samples were punched out from the sections located at a distance of 2.5 mm from the center of the annealed HPT disks, and they were subsequently ion-milled using a Gatan plasma ion polisher. The average grain size in each annealing condition was determined from TEM images using the modified line intercept method [25]. Each annealed disk was mechanically polished to a mirror-like quality, and the constituent phases were measured by an X'Pert PRO X-ray diffractometer employing Cu-Kα radiation.

The Vickers hardness of the polished disks was measured at the half-radius positions using a Zwick microhardness tester under a constant load of 500 gf and a dwell time of 15 s.

[1] In this work we take the atomic radius for metallic bonds to be representative of the atomic radius.

Each reported microhardness value was determined from an average of eight separate hardness measurements.

3. Results and analysis

3.1. Microstructure after annealing treatment

HPT processing at room temperature of the solution treated Mg-Gd-Y-Zn-Zr alloy produces a nanostructured supersaturated solid solution with a mean grain size of ~48 nm [24]. Fig. 1 shows the microstructure of the HPT-processed Mg-Gd-Y-Zn-Zr supersaturated alloy after annealing at 473 K and 573 K. In Fig. 1 (a–c), no apparent change in the grain size is observed in the sample annealed at 473 K, and the corresponding selected area electron diffraction (SAED) patterns exhibit continuous diffraction rings, further confirming the presence of nanograins with high-angle grain boundaries. As shown in Fig. 1(g) and (h), brighter Z-contrast is visible at grain boundaries, indicating that the distribution of the solute atoms is not uniform, i.e. segregation of solute atoms

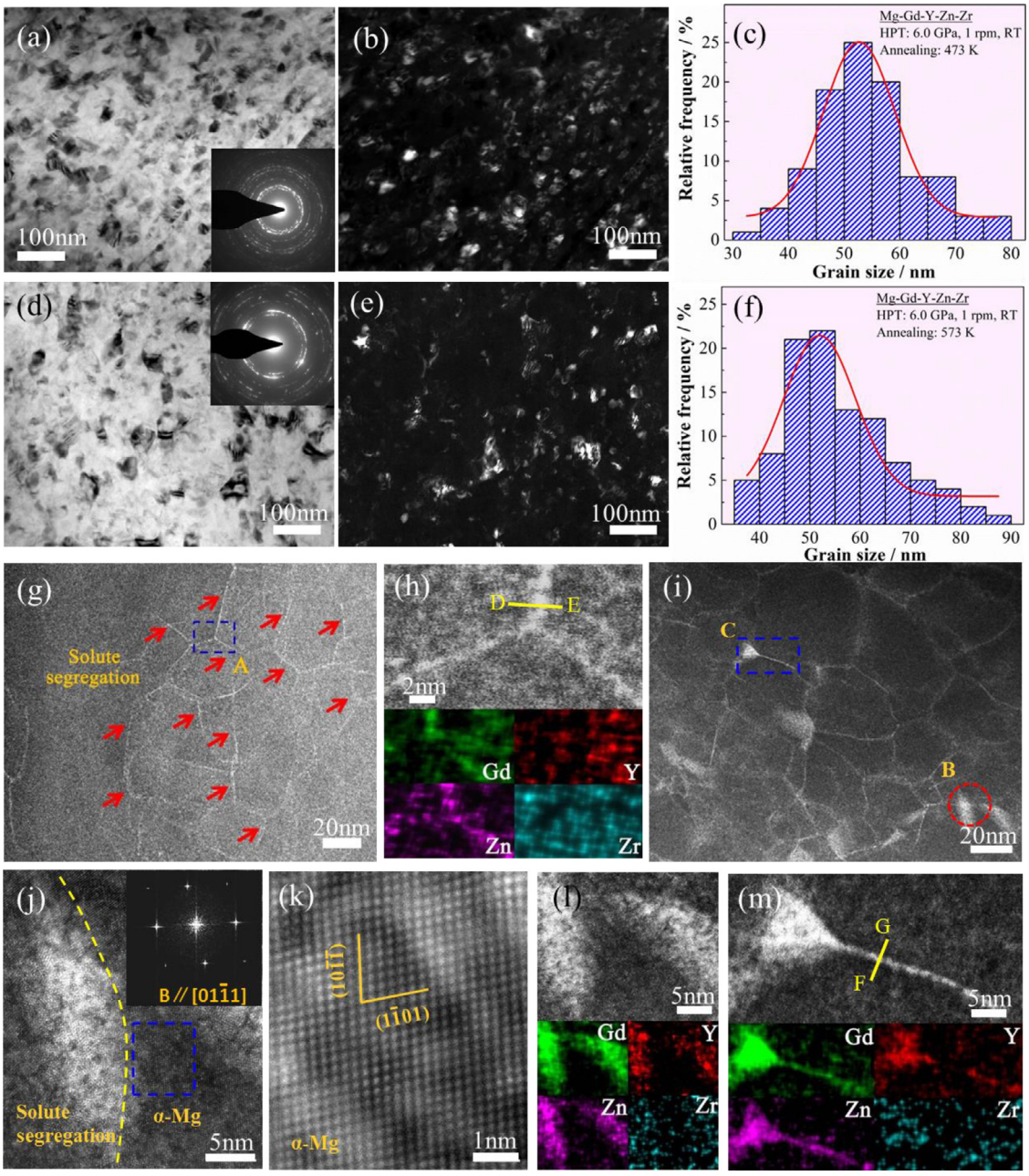

Fig. 1. Microstructure of the HPT-processed supersaturated Mg-Gd-Y-Zn-Zr alloy after annealing at 473 K (a, b, c, g, h) and 573 K (d, e, f, i, j, k, l, m): (a) and (d) TEM bright-field images and the corresponding SAED patterns inserted; (b) and (e) TEM dark-field images; (c) and (f) histograms of grain size distributions; (g) and (i) HAADF images; (h) the atomic resolved HAADF-STEM image and elemental mappings of region A in (g); (j) magnified HAADF-STEM image of the region B marked in (i) and the corresponding Fast Fourier Transform (FFT) image of α-Mg matrix inserted; (k) Inverse Fast Fourier Transform (IFFT) image of the region marked by blue dash square in (j); (l) and (m) atomic resolved HAADF-STEM images and elemental mappings of regions B and C marked in (i), respectively.

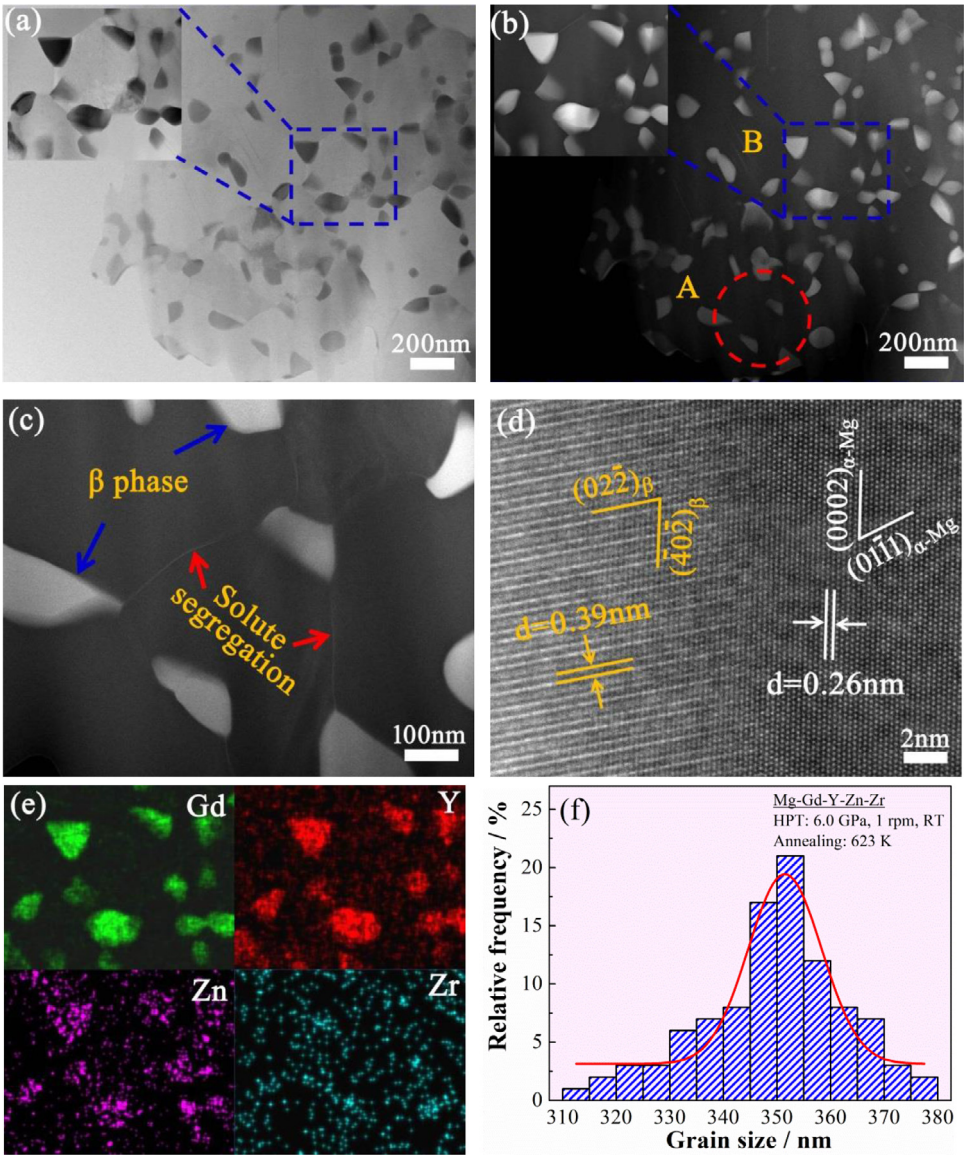

Fig. 2. Microstructure of the HPT-processed Mg-Gd-Y-Zn-Zr alloy followed by annealing at 623K: (a) TEM bright-field image; (b) HAADF-STEM image; (c) HAADF-STEM image of the region A marked in (b); (d) atomic resolved HAADF-STEM image of a precipitate along the grain boundary; (e) elemental mappings of region B marked in (b) and (f) histograms of grain size distributions.

has occurred during annealing at 473 K. After further increasing the annealing temperature up to 573 K grain growth is virtually undetectable, with an average grain size measured at ~55±4 nm (see Fig. 1(d–f)), and inhomogeneous diffraction contrast in grain interiors due to the high density of defects introduced during HPT [24,26]. As compared to the sample annealed at 473 K, more solute atoms have segregated at grain boundaries during annealing at 573 K, especially in the regions marked by B and C in Fig. 1(i). The magnified HAADF-STEM image of region B as shown in Fig. 1(j) further confirms the solute segregation at grain boundaries. The corresponding EDS mappings shown in Fig. 1(l) and (m) demonstrate these segregation areas contain Gd, Y and Zn, i.e. they are co-clusters containing the 3 main alloying elements with typical dimensions of a few nm. It is noted that apart from the Mg diffraction rings there are no diffraction spots from other phases in the samples annealed at both 473 K and 573 K (see the inserted SAED patterns in Fig. 1(a) and (d)), and correspondingly no precipitates are detected in bright field TEM imaging.

Fig. 2 shows the microstructure of the HPT-processed supersaturated Mg-Gd-Y-Zn-Zr alloy annealed at 623 K. The grain boundaries are well defined, indicating that the redistribution and annihilation of dislocations leads to relaxation of internal stresses. The average grain size is increased to ~350 nm (see Fig. 2(a), (b) and (f)). It is observed that second phase particles with a diameter of 90±10 nm are formed; they are distributed along the grain boundaries as well as at triple point junctions. The magnified HAADF-STEM image shown in Fig. 2(c) shows that as compared to the material annealed at the lower temperature of 573 K, only a small amount of solutes are segregated at grain boundaries. This suggests

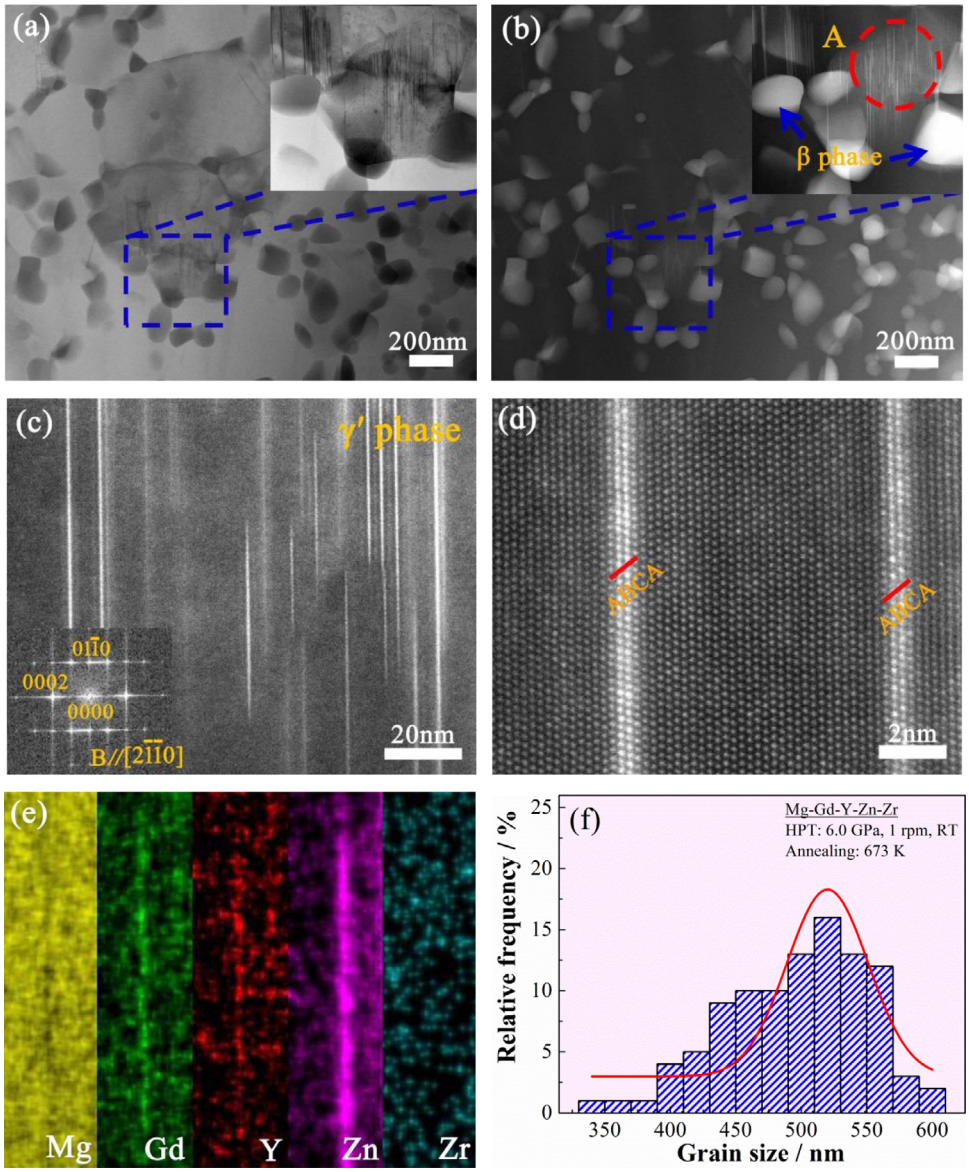

Fig. 3. Microstructure of the HPT-processed Mg-Gd-Y-Zn-Zr alloy after annealing at 673 K: (a) TEM bright-field image; (b) HAADF-STEM image; (c) HAADF-STEM image of the region A marked in (b) with the fast Fourier transform (FFT) image of the γ' phase lamellae inserted; (d) atomic resolved HAADF-STEM image of γ' phase and (e) elemental mappings of γ' phase and (f) histograms of grain size distributions.

that the second phase particles that formed have consumed the solute atoms that were present in the co-cluster regions and solute segregation at grain boundaries. The lattice parameters obtained from atomic resolved HAADF-STEM images and the elemental mappings in Fig. 2(d) and (e) indicates that these precipitates are the β phase (Mg_5RE type compounds, fcc structure, F4$\bar{3}$m, a=2.23 nm [27, 28]), and thermodynamic modelling using the PanMg database shows that for the present alloy the Mg_5RE phase is thermodynamically stable at temperatures below 650 K [29].

Fig. 3 shows the microstructure of the HPT-processed Mg-Gd-Y-Zn-Zr alloy after annealing at 673 K. Fig. 3(a), (b) and (f) show that the annealing at 673 K causes the average grain size to increase up to ~500 nm. The β phase particles at the grain boundaries coarsen slightly to 115±8 nm. It is interesting to note that lamella-shaped structures form inside the grains (see Fig. 3(c)); they precipitate on the basal plane of the Mg-rich matrix phase as shown in the FFT patterns. According to the atomic resolution HAADF-STEM image in Fig. 3(d) and corresponding EDS analysis in Fig. 3(e), these long lamella-shaped structures contain stacking faults (SFs) and are enriched with Zn and RE elements. These structures have been observed in other Mg-RE alloys and have been termed γ' phase precipitates; alternatively we might call them solute-enriched SFs, whilst also the term 'solute segregated SFs' has been used to describe these structures [30,31].

3.2. XRD analysis

Fig. 4 presents the XRD patterns of the HPT-processed Mg-Gd-Y-Zn-Zr alloy after annealing at various temperatures. For the samples annealed at 473 K and 573 K, all the XRD

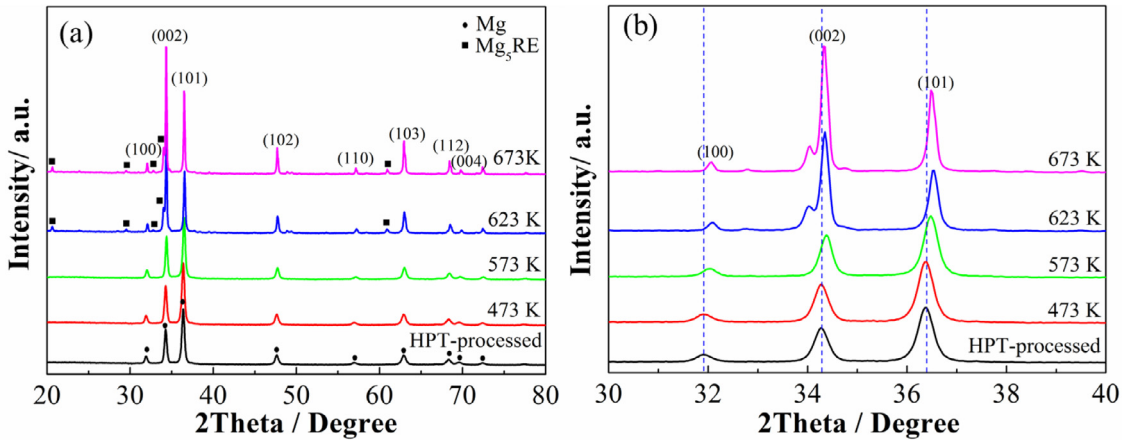

Fig. 4. (a) XRD patterns of HPT-processed and annealed Mg-Gd-Y-Zn-Zr alloys; (b) Section of XRD patterns in (a) in the range of 30°−40°.

peaks are due to the α-Mg phase, and with increasing annealing temperature the positions of peaks gradually shift to a larger angle (see Fig. 4(b)). This can be explained by depletion of solutes in the matrix due to the segregation at grain boundaries, which causes the lattice parameters of the α-Mg phase of the grain interior to decrease [18]. After annealing at 623 K, diffraction peaks of the β-Mg_5RE compound appear and they become sharper after annealing at 673 K, which is in agreement with TEM observation shown in Figs. 2 and 3. Fig. 4(b) shows that when the annealing temperatutre increases from 573 K to 673 K, the positions of the three main α-Mg peaks remain unchanged, suggesting all of the β phase forms from the solute segregation. Besides, after annealing treatments, the peaks of the Mg-rich phase become sharper, which is due to increase in grain size and reduction of the dislocation density owing to recovery and annihilation of dislocations. Recovery occurs especially at the higher temperatures of 623 K and 673 K.

3.3. Evolutions of hardness and grain size upon annealing

Fig. 5 shows the variations of hardness and average grain size of the HPT-processed Mg-Gd-Y-Zn-Zr alloy as a function of annealing temperature. In the low temperature region (473 K-573 K), hardness increases with increasing temperature, while there is almost no change in the mean grain size. Apparently the co-cluster formation near and solute segregation at grain boundaries (see Section 3.1) play an important role in hardness enhancement. The hardness reaches ~136 HV after annealing at 573 K, which is ~8% higher than that of the initial HPT-processed sample. At higher temperatures (623 K-673 K), dramatic grain growth occurs and the

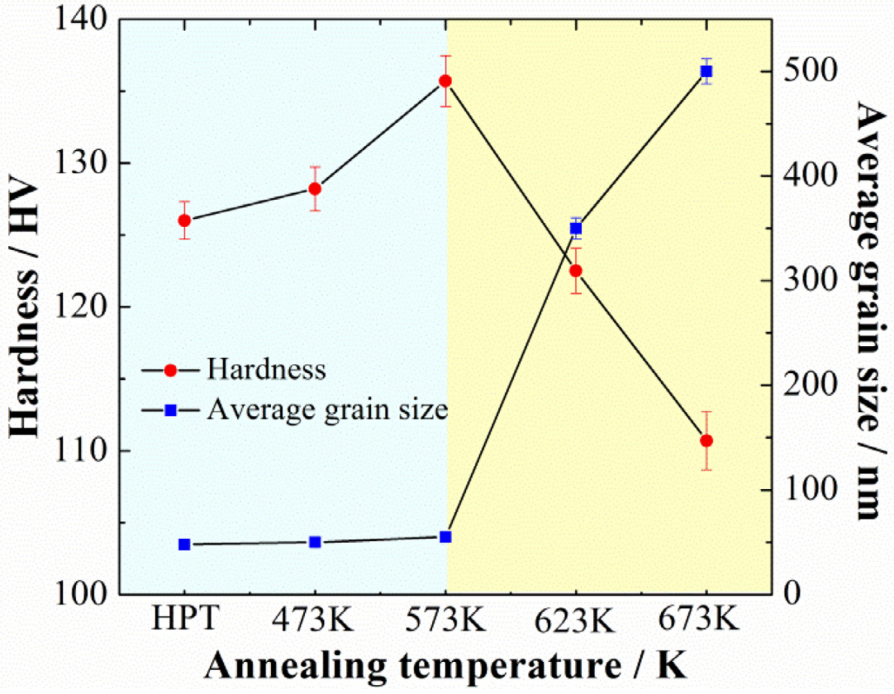

Fig. 5. Effect of annealing temperature on the average grain size and hardness variation for HPT-processed Mg-Gd-Y-Zn-Zr alloy.

hardness decreases. On the basis of TEM observations and XRD results, the reduced dislocation density is due to rearrangement and annihilation of dislocations with opposite signs during annealing.

4. Discussion

In this section we mainly wish to discuss the remarkable stability of the near nanosized grains up to 573 K, which approximately equates to 0.64 T_M, with T_M being the melting temperature (liquidus) of the alloy. As this is closely related to the clustering and segregation, these aspects will be discussed in Section 4.1. The mechanisms for the remarkable stability will be discussed in Section 4.2.

4.1. Clustering, segregation and phase transformations during annealing

Based on the above microstructure observations, the present results indicate that on annealing at temperatures up to 673 K in the HPT-processed Mg-Gd-Y-Zn-Zr supersaturated nanostructured material several unique phase transformations occur. Fig. 6 provides the schematic illustration of microstructure evolution of HPT-processed Mg-Gd-Y-Zn-Zr nanostructure during heat treatment under different conditions. Apart from the trend of grain growth, it also can be determined that the precipitation behavior strongly depends on the annealing temperatures. At the low temperature region of 473 K-573 K, solute co-clustering and segregation at GBs are generated, whereas the majority of alloying solutes are gradually transformed into equilibrium β-Mg_5RE phase distributed along GBs as well as at triple point junctions after annealing at 623 K. As the annealing temperature further enhanced to 673 K, all the solute segregation disappears instead of the appearance of lamella-like γ' phase precipitates within grains, while the β particles slightly coarsen. Accordingly, the precipitation behavior can be briefly summarized as follows:

473 K-573 K: α-Mg (ssss) $\rightarrow$ solute co-clustering and segregation at GBs

623 K: α-Mg (ssss) $\rightarrow$ solute co-clustering and segregation at GBs $\rightarrow$ β (fcc, Mg_5RE)

673 K: α-Mg (ssss) $\rightarrow$ β (fcc, Mg_5RE) + γ' (solute-enriched SFs)

A full understanding of the driving forces for clustering and segregation requires atomistic modeling; they depend for instance on elastic misfit (e.g. relative atomic size) and electron interactions. In fact, available evidences for the phenomenon of similar absolute magnitude co-clustered segregations are also found in the ternary alloys / quaternary alloys deformed by HPT processing, in which the atomic misfits of 10–20% of opposite with reference to parent phase matrix generally tend to cluster located at the defects [21,22]. Accordingly, we here focus on the relative atomic sizes of the atoms involved in a higher order system, as this appears to provide a valid explanation for the present multi-alloying element interactions, as well as many clustering effects in alloys observed in the literature [21,22]. In our present case, the atomic radius is 0.180 nm for Gd, 0.133 nm for Zn, and Y has an atomic size (radius 0.18 nm) similar to that of Gd. Therefore, the corresponding atomic misfitting strains with

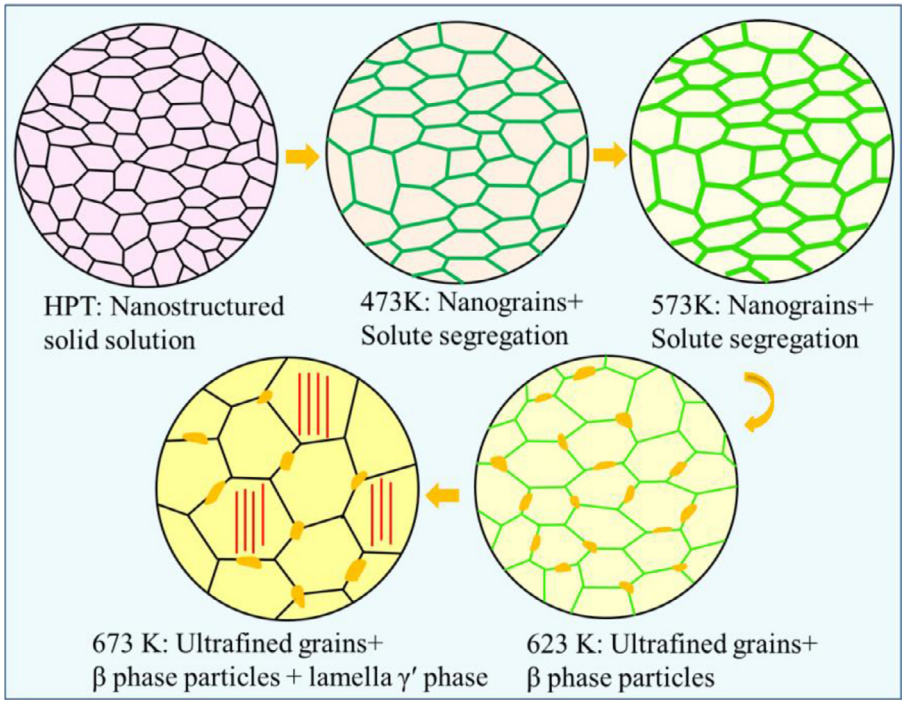

Fig. 6. Schematic illustration of microstructure evolution of HPT-processed Mg-Gd-Y-Zn-Zr nanostructure during heat treatment.

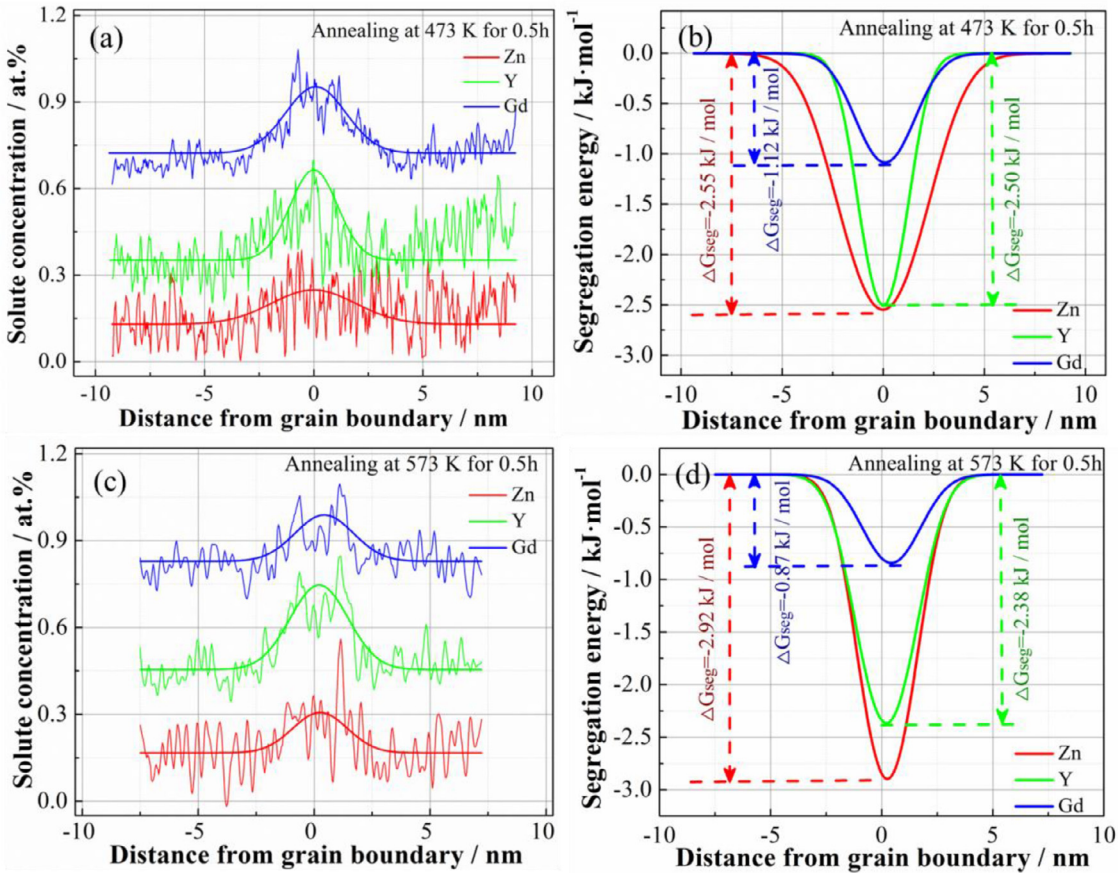

Fig. 7. (a) and (c) EDS line scanning profiles of the corresponding lines marked by "DE" and "FG" in Fig. 1(h) and (m), respectively; (b) and (d) Calculations of grain boundary segregation energies of Gd, Y and Zn solute atoms in α-Mg matrix using the Langmuir-McLean model plotted as a function of distance from the grain boundaries after annealing after 473 K and 573 K, respectively.

reference to Mg are +12.5% and −16.9% for the elements of RE and Zn, respectively. This suggests that within the Mg-rich phase, the presence of a RE atom with positive misfit causes a compression strain, whereas the presence of a Zn atom with a negative misfit causes an extension strain [2,18]. These differences will create a driving force for co-clustering of small and large solute atoms, and in line with observations in other ternary systems with negative and positive misfit atoms [21,22,32], we can expect clustering to occur. (In this sense our alloy is very different to binary Mg-RE alloys where segregation tendency is more limited and dependant on factors other than just the misfit [5].) It is noted that in line with the above interpretation, Zr, which has the same atomic radius as Mg, does not show a tendency for clustering with the other alloying elements, nor does it show GB segregation. (It should be noted that elastic misfit is only one of the factors promoting grain boundary segregation and a full explanation of the present observations requires further detailed analysis.)

In order to better explore the underlying principles that favor segregation, from the point of thermodynamics, the extent of solute segregation located at grain boundaries in polycrystalline alloys can be determined by the Gibbs free energy for GB segregation ($\triangle G_{Seg}$) [33]. Based on the classical Langmuir-McLean segregation isotherm theory, the distribution relation of solute atoms can be mathematically expressed as follows [33–36]:

$$\frac{X_{GB}}{1-X_{GB}} = \frac{X_{Bulk}}{1-X_{Bulk}} exp\left(\frac{-\Delta G_{Seg}}{RT}\right) \tag{1}$$

where X_{GB} and X_{Bulk} represent the solute concentration at GB and in the bulk, respectively, R is gas constant, and T is the temperature.

According to Eq. (1), it reveals that when the value of $\triangle G_{Seg}$ is negative, there is a driving force for favoring solutes to segregate at grain boundaries, thus causing a lower free energy of the system. Fig. 7(a) and (c) provide both the Zn and RE atomic concentration profiles across the grain boundaries after annealing at 473 K and 573 K, respectively, and thereby the corresponding free energy of segregation for each solute element can be roughly quantified using Eq. (1) against the distance from grain boundaries, as shown in Fig. 7(b) and (d). It is found that all the contents of solute segregation are increased when the annealing temperature is enhanced. Nevertheless, higher temperature is more likely favorable for the occurrence of Zn element occupied at grain boundaries as its $\triangle G_{Seg}$ becomes smaller, whereas the corresponding $\triangle G_{Seg}$ values of RE elements are slightly increased. Therefore, it

means that the tendency of solutes segregation is not only controlled by thermodynamics but also the kinetics factors.

Whilst the atomic misfit provides an important part of the driving force for clustering and segregation, the presence of a multitude of defects in the grain (i.e. dislocations, vacancies [37,38]) induced by HPT processing will enhance the diffusion rate [39], providing enhanced rate of segregation and co-clustering. The combination of high diffusion rate, small grain size and a driving force allows segregation and formation of co-clusters at grain boundaries [40]. The present experiments show that the rate of co-clustering and segregation increases with increasing temperature up to 573 K. After heat treatment at 623 K, segregation and co-clustering at the grain boundaries is much reduced, as Gd and Y are incorporated in the β (fcc Mg_5RE) phase. Apparently, nuclei of this equilibrium phase first become viable at this elevated temperature and growth of this equilibrium phase starts. After annealing at 673 K, no solute segregation is observed and most alloying atoms are incorporated into the equilibrium β phase along the grain boundaries and the γ' phase precipitates within grains.

Such γ' precipitation has also been reported during isothermal ageing at ~673 K of Mg-1Zn-2Gd (at.%) alloy, whilst no γ' was observed for ageing at low temperature of ~473 K [30]. It has been shown that the simultaneous addition of RE and Zn into the Mg matrix can decrease the stacking fault energy (SFE), facilitating the formation of planar faults on $(0001)_{\alpha-Mg}$ planes [41]. Since the solubility limit of RE and Zn increases with increasing temperature, higher concentration of solutes remaining in the Mg matrix will promote the precipitation of γ' phase [31]. It also should be pointed out that γ' precipitates can transform into a long period stacking ordered (LPSO) phase with increasing annealing time at 673 K [30].

The phase transformations on annealing of the present nanostructured, supersaturated Mg-Gd-Y-Zn-Zr alloy are quite different from that of Mg-RE alloys with coarse microstructure [42,43]. For example, at the very early stage of ageing (0.5 h) at 523 K, many small spheroidal β'' particles with a diameter less than ~10 nm precipitated within grains of a Mg-10Gd-3Y-0.4Zr (wt.%) alloy [44]. In the Mg-15Gd (wt.%) alloy, the isochronal annealing carried out in steps of 30 K/0.5 h led to precipitation of coherent rod-like β'' phase at 473 K, and precipitation of semicoherent β' phase in the grain interior at 513 K and incoherent β phase after annealing up to 693 K [42]. When the same heating processing was performed on an Mg-3Y-2.5Nd (wt.%) alloy, plate-like β'' phase formed at 513 K which on further annealing up to 633 K transformed into the stable β phase without evidence of β_1 phase [43].

One factor explaining the difference in precipitation behavior in our nanostructured, supersaturated Mg-Gd-Y-Zn-Zr alloy is that with grain size refined down to the nanoscale, the high grain boundary volume fraction will govern the precipitation behaviors [17]. The shorter diffusion paths in combination with high vacancy concentrations in our HPT processed nanostructured alloy allow rapid formation of clusters and segregation at low temperatures (<623 K) and GB precipitates at more elevated temperatures, with the attendant solute depletion of the grain interiors precluding precipitation in the grain interiors.

4.2. Mechanisms of grain growth suppression in the Mg-Gd-Y-Zn-Zr alloy

Fig. 8 exhibits a comparison of thermal stability of the grain size for various SPD-processed Mg-based alloys annealed at temperatures up to 673 K. This figure reveals that for conventional RE-free Mg-based alloys processed by various SPD methods, the annealing response is very sensitive to the deformation parameters and temperature, and in all these

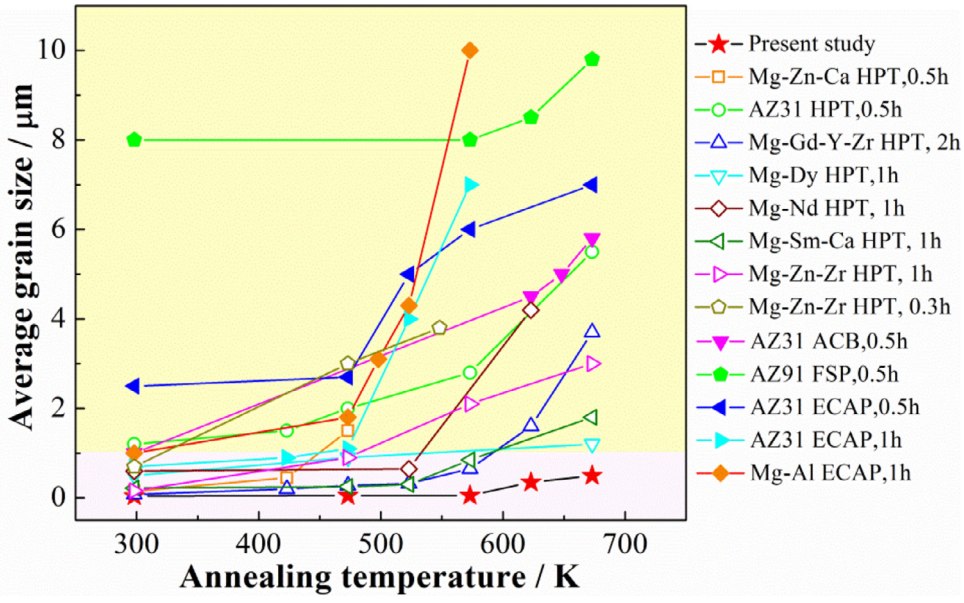

Fig. 8. Comparison of the thermal stability of different SPD-processed Mg-based alloys (ACB, FSP and ECAP represent accumulative compression bonding, friction stir processing and equal channel angular pressing, respectively [9–12,45–54].

RE-free alloys pronounced grain growth occurs after annealing at temperature above 473 K [9–12,45–50]. In all these cases the grain sizes of SPD-processed RE-free Mg alloys grow beyond 1 μm on exposure at 473 K. In contrast, the present HPT-processed high RE Mg-Gd-Y-Zn-Zr alloy retains nanosized grains up to 573 K and grain growth at higher temperatures is much more limited with grain size remaining well below 1 μm, which also exhibits a distinguished superior thermal stability to the other HPT-deformed Mg-RE alloys [51–54]. As shown in Fig. 8, it is also worth noting that the initial smallest grain size in present work having a higher thermal stability clearly breaks away from the normal "smaller-less-stable" trend. In other reported work on SPD processing of Mg-RE alloys (e.g. by ECAP, repetitive upsetting (RU) and cyclic expansion extrusion (CEE)) with exposure during or after processing at or beyond 573 K, the grain size was always found to be larger than ~300 nm [39,55–57]. Thus the stability of grain refinement of the present alloy/processing combination, allowing grain size to be limited to 55 nm after exposure at 573 K, appears to be generally one order of magnitude better than for other SPD-processed Mg-RE type alloys, and 2 orders of magnitude better than SPD-processed RE-free Mg alloys. (For further comparison, we also note that an Mg-5Ti (at.%) sample produced by mechanically alloying showed an ultrafine grain size of 145 nm after annealing at 350 °C for 1 h [13]. However, the sample showed abnormal grain growth and the formation of a bimodal microstructure.

Clearly the present HPT-processed high RE Mg-Gd-Y-Zn-Zr alloy has a resistance to grain coarsening that outperforms all other reported conventionally processed and SPD processed Mg alloys. To be able to fully exploit this finding it is important to determine the mechanisms responsible for this. The main mechanisms for limiting grain growth as mentioned in the literature are (i) triple junction effect [34,58,59], (ii) grain boundary pinning by second phase particles or precipitates [60], (iii) solute drag [61,62], (iv) thermodynamic stabilizing of the fine grains through segregation of solutes at the grain boundaries [63–65]. The latter mechanism has recently attracted considerable interest. It considers that segregation and clustering of solutes at or near the grain boundaries provides a strong reduction in free energy of the material. At a certain (relatively low) temperature, a thermally stable (or metastable) grain size may be achieved when the driving forces for changes in grain size reach a balance [66,67], i.e. in such a situation a reduction in the density of grain boundaries (i.e. grain growth) is thermodynamically not possible as it would increase the free energy.

We here will consider each of the four mechanisms mentioned above, firstly focusing on the temperature range up to 573 K where ultra-stable near-nanoscale grains are observed.

In several works on SPD processed Mg based alloys it has been suggested that precipitates play an important role in limiting grain growth. However, in the temperature range up to 573 K this is not the case for our ultra-stable Mg-8.2Gd-3.8Y-1.0Zn-0.4Zr (wt.%) alloy because the present TEM work clearly shows that no precipitates are present at the grain boundaries in this temperature range. Evidently, solution treatment was effective and subsequent HPT followed by heat treatment up to 573 K did not cause nucleation of any precipitate discernable by TEM observations. Both solute drag caused by the segregation of Gd, Y and Zn and thermodynamic stabilizing of the fine grains through segregation of solutes at the grain boundaries are a potential mechanism operating in the temperature range up to 573 K. In line with that interpretation, significant grain growth starts after annealing at 623 K when grain boundary segregation disappears and solute atoms are incorporated in the precipitates that form at this temperature. Additionally, the triple junction may also slow down the grain growth since the triple junction moves very slow and it effectively limits the grain growth when the grain size is very small. There exists a critical volume fraction of the triple junction which restrains the grain growth [58,59]. For instance, volume fraction of the triple junction of a metal with grain size of 10 nm is about 3%. In this work, the grain size before annealing is 48 nm, which corresponds to a volume fraction of 0.1% according to Eq. (7) proposed in [68]. Thus, the effect of the triple junctions in the present materials is thought to be limited. Nevertheless, any effect of triple junctions in slowing down grain growth will be enhanced by the segregation and co-clustering at the triple junctions causing a contribution to the thermodynamic stabilizing. So at this stage the mechanism depends on competition of grain growth, grain boundary segregation and precipitation, and change in mechanisms is most likely to be initiated by the formation of viable nuclei of the precipitating phase, which will then start diffusion of solutes to the growing precipitates, triggering a reduction in the solute drag and thermodynamic stabilization effects.

With increasing temperature, precipitation processes start to influence the free energy changes which will influence grain boundary segregation and grain growth. At a relatively high temperature, 623 K in the present work, segregation and clustering near grain boundaries become thermodynamically unstable due to the formation of precipitates. As a result, the free energy associated with the grain boundary per unit area or per unit volume increases due to the boundary losing the segregated atoms and grain growth re-gains a net positive driving force. Even though grain growth now does occur, the grain size of the present Mg-Gd-Y-Zn-Zr alloy is still limited to 350 nm after annealing at 623 K. This is thought to be due mainly to the Zener pinning effect of the precipitates.

To further analyse the mechanisms we will employ Burke and Turnbull's equation for grain growth [69]:

$$D^n - D_0^n = kt \tag{2}$$

where D and D_0 are the current and initial values of the grain size, respectively, n is the grain growth empirical exponent, t is fixed annealing time (in this case fixed at 0.5 h), and k is a temperature-dependant kinetic constant that can be expressed by an Arrhenius type Eq. (3):

$$k = k_0 \exp\left(-\frac{E_a}{RT}\right) \tag{3}$$

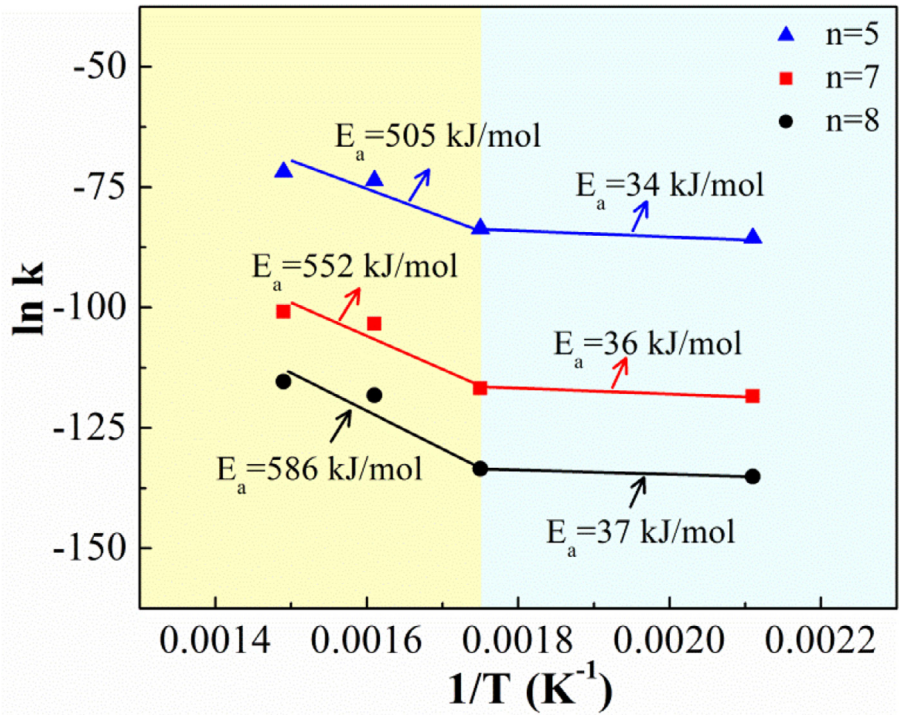

Fig. 9. Plot of ln$k$ against 1/T to estimate the activation energy for grain growth of the HPT-processed Mg-Gd-Y-Zn-Zr alloy.

where k_0 is a pre-exponential constant, E_a is the activation energy for grain growth, T is the annealing temperature and R is the universal gas constant. Based on Eqs. (2) and (3), E_a can be estimated by the slope of a plot of ln k against (1/T) and such a plot is shown in Fig. 9. The value of grain growth exponent n represents the resistance to grain boundary motion in the presence of impurity or alloying elements in solid solution, which is usually influenced by several factors such as compositional parameters, dislocation substructure, the solute drag and microstructure heterogeneities [70,71]. For ultrafine-grained Mg-based alloys and Mg-based composites prepared by different SPD routes, the values of n are mainly taken as 2, 5, 7 and 8 [9,14,45,46,70–73]. In the idealized case of an infinite, defect-free crystal the grain growth exponent should be 2, as grain growth should be a parabolic function in which the driving pressure is only associated with the curvature of the boundary [69]. However, due to the presence of various microstructural factors affecting grain growth kinetics in real processed materials, higher values of n ($n \geq 5$) have been applied. In order to make comparison with other studies of SPD-processed Mg-based alloys, three different values of 5, 7 and 8 are used to evaluate the (apparent) activation energy in the present study.

In Fig. 9, it can be seen that for each value of n the HPT-processed Mg-Gd-Y-Zn-Zr alloy has two main distinguishable grain growth regimes with different activation energies. For the low temperature region (473 K-573 K), where hardly any grain growth was detected, the activation energy is very low at about 35±2 kJ/mol, which is much lower than the activation energy of grain boundary diffusion (Q_{gb}=92 kJ/mol) and lattice self-diffusion (Q_L=135 kJ/mol) in pure Mg [74]. The main reason for this very low activation energy is the near total suppression of grain growth due to the mechanisms related to segregation and clustering, as described above. As solute drag should be governed by diffusion of solutes [75,76], such low activation energy suggests that solute drag on its own cannot explain the limited grain growth in the low temperature range, indicating that thermodynamic stabilizing of the fine grains is the main factor. For the high temperature region (623 K-673 K) an exceptionally high apparent activation energy (505–586 kJ/mol) is found, which is larger than those of other SPD-processed UFG Mg-based alloys under similar annealing conditions [9,14,70–72]. This very high activation energy, which is 3 to 4 time larger than that for self-diffusion or solute diffusion, indicates that in this temperature range the kinetics are not driven by a single process, and instead are driven by a chain of linked interacting processes. As discussed above these linked processes are thought to be the nucleation and growth of precipitates, which causes the removal of solute segregation and clustering (near grain boundaries) and the resulting shift from a thermodynamic (and segregation) controlled suppression of grain growth to grain boundary pinning by precipitates, e.g. by β phase and γ' phase which form at these at higher temperatures.

4.3. Effect of annealing on hardness evolution

Upon isochronal annealing at different temperatures, the hardness increases with the increase of temperature, reaching a peak at 573 K, and then gradually decreases. This is quite different from the reported SPD-processed conventional Mg-based alloys, in which the hardness decreases monotonously

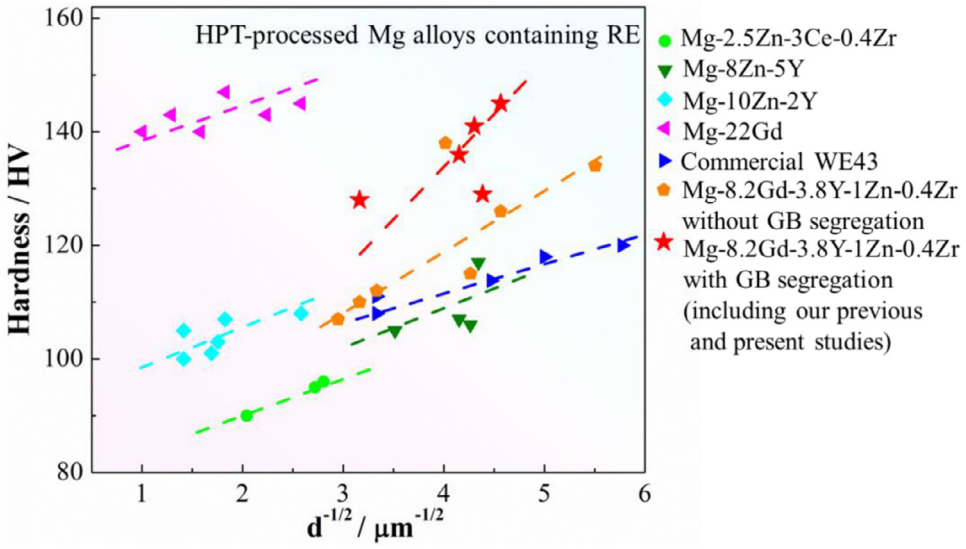

Fig. 10. Comparisons of the Hall-Petch relation plots with the Hardness as a function of reciprocal square root of grain size of various HPT-processed Mg alloys containing RE atoms reported in literatures [18,24,26,39,77–83] and present work.

with the temperature increasing [45,47,48,71]. Such softening in SPD-processed conventional Mg-based alloys is a consequence of the unavoidable coarsening of the grain structure and reduction in dislocation density at elevated temperatures. In the present work on HPT-processed Mg-Gd-Y-Zn-Zr is obviously deviated from the general trend of ordinary Mg alloys, i.e. the hardness gradually increases with increasing temperature in the first stage, whilst the grain size is stable. At this stage, two competitive processes may occur. One is the softening effect arising from static recovery, i.e. the annihilation and rearrangement of dislocations. The other is hardening due to the introduction of solute segregation and solute co-clustering at or near grain boundaries [18]. The hardness reaches a maximum of 136 HV after annealing at 573 K, indicating that the contribution of solute segregation and solute co-clustering at or near grain boundaries dominates. Besides, in order to evaluate the effects of solute segregation on the hardness enhancement, the comparisons of the Hall-Petch (H-P) relation plots of various HPT-processed Mg alloys containing RE atoms are given in Fig. 10. It is evident that as compared to the counterparts lacking of solute segregation [24,26,39,77–83], the Mg-RE nanostructures with solute segregation possess the largest positive H-P slope with the relatively finer grain size, further implying that the introduction of solute segregation characteristics brings about better hardening effects when the grain refinement into similar nanoscale. By contrast, in the temperature range of 623 K-673 K, a second stage occurs in which softening and grain growth is observed. Moreover, the coarse incoherent β-Mg_5RE phase, which is usually considered to have a very limited strengthening effect [18], is generated at the expense of the solute segregation. Therefore, the hardness evolution during annealing is closely associated with the grain growth and phase transformation. In addition, unavoidable annealing of dislocations also reduces hardness. It is anticipated that such HPT-processed Mg-RE-Zn structure with a high hardness and a superior thermal stability would provide an approach of structure design to overcome the trade-off between strength and thermal stability of wrought Mg alloys.

5. Conclusions

In this study, a HPT-processed Mg-8.2Gd-3.8Y-1.0Zn-0.4Zr (wt.%) nanostructured material with supersaturated Mg-rich phase was subjected to isochronal annealing at different temperatures. The grain growth, phase transformations and hardness evolution were evaluated. The main conclusions are summarized as follows:

(1) At low temperatures of 473 K and 573 K, no significant change in grain size is observed with an average value around 50 nm. At 623 K and 673 K grain growth to a mean size of ~350 nm and ~500 nm occurs, respectively. For all the annealed Mg-Gd-Y-Zn-Zr samples, the grain growth is restricted to below 1 μm, which is much smaller than those of the other SPD-processed conventional Mg-based alloys.
(2) At the low temperature region of 473 K-573 K, solute segregation forms at the grain boundaries, but after annealing at 623 K most of these solutes are transformed into equilibrium β-Mg_5RE phase distributed along grain boundaries as well as at triple point junctions. When the temperature is increased to 673 K, the β particles coarsen slightly, and all the solute segregation disappears, being replaced with lamella-like γ' phase precipitates within grains. The phase transformations on annealing of nanostructured Mg-Gd-Y-Zn-Zr alloy are quite different from the other Mg-RE alloys with coarse microstructure, which is attributed to the increased grain boundary volume fraction induced by HPT deformation.

(3) The present Mg-Gd-Y-Zn-Zr alloy exhibits an excellent thermal stability. The developed nanostructure in HPT-processed Mg-Gd-Y-Zn-Zr alloy is retained up to 573 K, whereas other SPD-processed conventional Mg-based alloys show a rapid grain growth at a temperature of 473 to 573 K. The improved stability is attributed to the formation of co-clusters near and segregation at grain boundaries, which cause a thermodynamic stabilization of grain size. Also at 623 K and 673 K grain growth in the present HPT-processed Mg-Gd-Y-Zn-Zr alloy is reduced as compared to SPD-processed conventional Mg-based alloys. This can be explained by the Zener pinning effect of numerous thermostable β particles at grain boundaries, which leads to a high grain growth activation energy at elevated temperatures.

(4) With increasing temperature the hardness of HPT-processed Mg-Gd-Y-Zn-Zr alloy initially increases, reaching a maximum at 573 K. At higher annealing temperatures hardness gradually decreases. This hardness evolution is different from those reported for SPD-processed conventional Mg-based alloys, in which the hardness reduced monotonously with increasing temperature. This difference is mainly ascribed to the hardening caused by the formation of solute segregation and formation of co-clusters at or near grain boundaries and the suppression of grain growth.

Conflict of interest statement

We declare that we have no commercial or associative interest that represents a conflict of interest in connection with the work submitted.

Acknowledgments

This work was supported by National Natural Science Foundation of China (No. U21A2047 and 51971076), China Postdoctoral Science Foundation (Grant No. 2019M653599) and Guangdong Basic and Applied Basic Research Foundation (No. 2019A1515110289).

References

[1] S.V.S. Prasad, S.B. Prasad, K. Verma, R. KumarMishra, V. Kuma, S. Singh, J. Magnes. Alloy 10 (2022) 1–61.
[2] J.S. Xie, J.H. Zhang, Z.H. You, S.J. Liu, K. Guan, R.Z. Wu, J. Wang, J. Feng, J. Magnes. Alloy 9 (2021) 41–56.
[3] R. Alizadeh, R. Mahmudi, A.H.W. Ngan, T.G. Langdon, J. Mater. Sci. 50 (2015) 4940–4951.
[4] C.J. Wang, J.W. Kang, K.K. Deng, K.B. Nie, W. Liang, W.G. Li, J. Magnes. Alloy 8 (2020) 441–451.
[5] I. Basu, K.G. Pradeep, C. Mießen, L.A. Barrales-Mora, T. Al-Samman, Acta Mater. 116 (2016) 77–94.
[6] M.G. Jiang, C. Xu, H. Yan, T. Nakata, Z.W. Chen, C.S. Lao, R.S. Chen, S. Kamado, E.H. Han, J. Magnes. Alloy 9 (2021) 1797–1805.
[7] M.K. Naeini, M. Sedighi, R. Hashemi, J. Magnes. Alloy 10 (2022) 938–955.
[8] D.A. Basha, R. Sahara, H. Somekawa, J.M. Rosalie, A. Singh, K. Tsuchiya, Scr. Mater. 124 (2016) 169–173.
[9] H.K. Kim, J. Mater. Sci. 39 (2004) 7107–7109.
[10] H.K. Lin, J.C. Huang, T.G. Langdon, Mater. Sci. Eng. A 402 (2005) 250–257.
[11] K. Matsubara, Y. Miyahara, Z. Horita, T.G. Langdon, Acta Mater. 51 (2003) 3073–3084.
[12] V. Jain, R.S. Mishra, Gouthama, J. Mater. Sci. 48 (2013) 2635–2646.
[13] X.C. Cai, B.R. Sun, Y. Liu, N. Zhang, J.H. Zhang, H. Yu, J.Y. Huang, Q.M. Peng, T.D. Shen, Mater. Sci. Eng. A 717 (2018) 144–153.
[14] M. Roostaei, M. Shirdel, M.H. Parsa, R. Mahmudi, H. Mirzadeh, Mater. Charact. 118 (2016) 584–592.
[15] V. Jain, R.S. Mishra, R. Verma, E. Essadiqi, Scr. Mater. 68 (2013) 447–450.
[16] J. Čížek, I. Procházka, B. Smola, I. Stulíková, R. Kužel, Z. Matěj, V. Cherkaska, R.K. Islamgaliev, O. Kulyasova, Mater. Sci. Eng. A 462 (2007) 121–126.
[17] X.H. Yang, K. Li, X.H. An, S. Ni, W.F. Wei, Y. Du, M. Song, J. Alloy. Compd. 695 (2017) 2238–2245.
[18] W.T. Sun, X.G. Qiao, M.Y. Zheng, C. Xu, S. Kamado, X.J. Zhao, H.W. Chen, N. Gao, M.J. Starink, Acta Mater. 151 (2018) 260–270.
[19] G.E. Totten, D.S. MacKenzie, Handbook of Aluminum (Eds.), Marcel Dekker, NY, USA, 2003.
[20] I. Sabirov, M.Yu. Murashkin, R.Z. Valiev, Mater. Sci. Eng. A 560 (2013) 1–24.
[21] M.J. Starink, L.F. Cao, P.A. Rometsch, Acta Mater. 60 (2012) 4194–4207.
[22] Y.D. Zhang, S.B. Jin, P.W. Trimby, X.Z. Liao, M.Y. Murashkin, R.Z. Valiev, J.Z. Liu, J.M. Cairney, S.P. Ringer, G. Sha, Acta Mater. 162 (2019) 19–32.
[23] N. Balasubramani, G. Wang, M.A. Easton, D.H. StJohn, M.S. Dargusch, J. Magnes. Alloy 9 (2021) 829–839.
[24] W.T. Sun, X.G. Qiao, M.Y. Zheng, C. Xu, N. Gao, M.J. Starink, Mater. Des. 135 (2017) 366–376.
[25] W. Yang, G.F. Quan, B. Ji, Y.F. Wan, H. Zhou, J. Zheng, D.D. Yin, J. Magnes. Alloy 10 (2022) 195–208.
[26] W.T. Sun, C. Xu, X.G. Qiao, M.Y. Zheng, S. Kamado, N. Gao, M.J. Starink, Mater. Sci. Eng. A 700 (2017) 312–320.
[27] C. Xu, M.Y. Zheng, K. Wu, E.D. Wang, G.H. Fan, S.W. Xu, S. Kamado, X.D. Liu, G.J. Wang, X.Y. Lv, J. Alloy. Compd. 550 (2013) 50–56.
[28] J.M. Meier, J.S. Miao, S.M. Liang, J. Zhu, C. Zhang, J. Caris, A.A. Luo, J. Magnes. Alloy 10 (2022) 689–696.
[29] W.T. Sun, X.G. Qiao, M.Y. Zheng, N. Hu, N. Gao, M.J. Starink, Mater. Sci. Eng. A 738 (2018) 238–252.
[30] M. Yamasaki, M. Sasaki, M. Nishijima, K. Higara, Y. Kawamura, Acta Mater. 55 (2007) 6798–6805.
[31] J. Zheng, Z.M. Yan, J.S. Ji, Y.S. Shi, H. Zhang, Z.M. Zhang, Y. Xue, Effect of heat treatment on mechanical properties and microstructure evolution of Mg-9.5Gd-4Y-2.2Zn-0.5Zr alloy, J. Magnesium Alloy doi:10.1016/j.jma.2021.05.018.
[32] J.F. Nie, K. Oh-ishi, X. Gao, K. Hono, Acta Mater. 56 (2008) 6061–6076.
[33] W. Xu, B. Zhang, K. Du, X.Y. Li, K. Lu, Acta Mater. 226 (2022) 117640.
[34] N. Tuchinda, C.A. Schuh, Acta Mater. 226 (2022) 117614.
[35] D. McLean, Grain Boundaries in Metals, Monographs on the Physics and Chemistry of Materials, Clarendon Press, 1957.
[36] I. Basu, M. Chen, J. Wheeler, R.E. Schäublin, J.F. Löffler, Segregation-driven exceptional twin-boundary strengthening in lean Mg-Zn-Ca alloys, Acta Mater. doi:10.1016/j.actamat.2022.117746.
[37] X.Q. Liu, X.G. Qiao, R.S. Pei, Y.Q. Chi, L. Yuan, M.Y. Zheng, Role of extrusion rate on the microstructure and tensile properties evolution of ultrahigh-strength low-alloy Mg-1.0Al-1.0Ca-0.4Mn (wt.%) alloy, J. Magnesium Alloy doi:10.1016/j.jma.2021.05.010.
[38] D.A. Basha, R. Sahara, H. Somekawa, A. Singh, K. Tsuchiya, Mater. Sci. Eng. A 703 (2017) 54–67.
[39] J. Čížek, P. Hruška, T. Vlasák, M. Vlček, M. Janeček, P. Minárik, T. Krajňák, M. Šlapáková, M. Dopita, R. Kužel, T. Kmječ, J.G. Kim, H.S. Kim, Mater. Sci. Eng. A 704 (2017) 181–191.
[40] S.K. Das, Y.B. Kang, T.K. Ha, I.H. Jung, Acta Mater. 71 (2014) 164–175.

[41] I.H. Jung, M. Sanjari, J. Kim, S. Yue, Scr. Mater. 102 (2015) 1–6.
[42] P. Vostrý, B. Smola, I. Stuíková, F. von Buch, B.L. Mordike, Phys. Status Solidi 175 (1999) 491–500.
[43] V. Neubert, I. Stulíková, B. Smola, B.L. Mordike, M. Vlach, A. Bakkar, J. Pelcová, Mater. Sci. Eng. A 462 (2007) 329–333.
[44] S.M. He, X.Q. Zeng, L.M. Peng, X. Gao, J.F. Nie, W.J. Ding, J. Alloy. Compd. 421 (2006) 309–313.
[45] H.K. Kim, W.J. Kim, Mater. Sci. Eng. A 385 (2004) 300–308.
[46] J.J. Ma, X.Y. Yang, Q.H. Huo, H. Sun, J. Qin, J. Wang, Mater. Des. 47 (2013) 505–509.
[47] O.B. Kulyasova, R.K. Islamgaliev, Y.H. Zhao, R.Z. Valiev, Adv. Eng. Mater. 17 (2015) 1738–1741.
[48] L.R.C. Malheiros, R.B. Figueiredo, T.G. Langdon, J. Mater. Res. Technol. 4 (2015) 14–17.
[49] S.A. Torbati-Sarraf, S. Sabbaghianrad, T.G. Langdon, Adv. Eng. Mater. 20 (2018) 1700703.
[50] A.P. Carvalho, R.B. Figueiredo, Adv. Eng. Mater. (2021) 2100846.
[51] L. Tang, Y. Zhao, R.K. Islamgaliev, R.Z. Valiev, Y.T. Zhu, J. Alloy. Compd. 721 (2017) 577–585.
[52] A. Hanna, H. Azzeddine, Y. Huang, D. Bradai, J.M. Cabrera, T.G. Langdon, Mater. Charact. 151 (2019) 519–529.
[53] S. Tighiouaret, R. Lachhab, A. Hanna, H. Azzeddine, Y. Huang, T. Baudin, A.L. Helbert, F. Brisset, D. Bradai, T.G. Langdon, Adv. Eng. Mater. 21 (2019) 1900801.
[54] X.H. Liu, R. Xu, J. Mater. Eng. Perform. (2021) 1–9.
[55] P. Minárik, J. Veselý, J. Čížek, M. Zemková, T. Vlasák, T. Krajňák, J. Kubásek, R. Král, D. Hofman, J. Stráská, Mater. Charact. 140 (2018) 207–216.
[56] A. Soheil, F. Ghader, Int. J. Min. Metall. Mater. 25 (2018) 672–681.
[57] H. Zhou, H.Y. Ning, X.L. Ma, D.D. Yin, L.R. Xiao, X.C. Sha, Y.D. Yu, Q.D. Wang, Y.S. Li, J. Mater. Sci. Technol. 34 (2018) 1067–1075.
[58] B. Zhao, G. Gottstein, L.S. Shvindlerman, Acta Mater. 59 (2011) 3510–3518.
[59] G. Gottstein, L.S. Shvindlerman, B. Zhao, Scr. Mater. 62 (2010) 914–917.
[60] T. Gladman, Proc. R. Soc. Lond. A 294 (1966) 298–309.
[61] M. Hillert, Acta Mater. 52 (2004) 5289–5293.
[62] J.W. Cahn, Acta Metall. 10 (1962) 789–798.
[63] T. Chookajorn, H.A. Murdoch, C.A. Schuh, Science 337 (2012) 951–954.
[64] A.R. Kalidindi, C.A. Schuh, Acta Mater. 132 (2017) 128–137.
[65] W.T. Xing, A.R. Kalidindi, D. Amram, C.A. Schuh, Acta Mater. 161 (2018) 285–294.
[66] H.A. Murdoch, C.A. Schuh, Acta Mater. 61 (2013) 2121–2132.
[67] T. Chookajorn, C.A. Schuh, Acta Mater. 73 (2014) 128–138.
[68] Y. Chen, C.A. Schuh, J. Appl. Phys. 101 (2007) 063524.
[69] J.E. Burke, D. Turnbull, Prog. Met. Phys. 3 (1952) 220–292.
[70] F. Khan MD, S.K. Panigrahi, Mater. Sci. Eng. A 675 (2016) 338–344.
[71] J. Stráská, M. Janeček, J. Čížek, J. Stráský, B. Hadzima, Mater. Charact. 94 (2014) 69–79.
[72] Y. Radi, R. Mahmudi, Mater. Sci. Eng. A 527 (2010) 2764–2771.
[73] M.A. Thein, L. Lu, M.O. Lai, Compos. Sci. Technol. 66 (2006) 531–537.
[74] O.D. Sherby, J. Weertman, Acta Metall. 27 (1979) 387–400.
[75] D. Fan, S.P. Chen, L.Q. Chen, J. Mater. Res. 14 (1999) 1113–1123.
[76] H. Sun, C. Deng, Comput. Mater. Sci. 93 (2014) 137–143.
[77] M. Janecek, P. Minarik, T. Krajnak, K. Vaclavova, J. Strasky, K. Cizek, M. Vicek, J. Vesely, J.G. Kim, H.S. Kim, Adv. Mater. Lett. 8 (2017) 897–904.
[78] W.T. Sun, X.G. Qiao, M.Y. Zheng, Y. He, N. Hu, C. Xu, N. Gao, M.J. Starink, Mater. Sci. Eng. A 728 (2018) 115–123.
[79] K. Bryła, J. Morgiel, M. Faryna, K. Edalati, Z. Horita, Mater. Lett. 212 (2018) 323–326.
[80] E.A. Lukyanova, N.S. Martynenko, I. Shakhova, A.N. Belyakov, L.L. Rokhlin, S.V. Dobatkin, Y.Z. Estrin, Mater. Lett. 170 (2016) 5–9.
[81] E.A. Lukyanova, N.S. Martnenko, E.V. Li, V.N. Serebryany, A.N. Belyakov, L.L. Rokhlin, S.V. Dobatkin, Y.Z. Estrin, Int. Sci. J. Mater. Sci. 3 (2017) 161–164.
[82] Y.S. Li, J.H. Wang, R. Xu, Vacuum 178 (2020) 109396.
[83] P. Jenei, J. Gubicza, E.Y. Yoon, H.S. Kim, J. Alloy. Compd. 539 (2012) 32–35.